


 Cite this: *RSC Adv.*, 2022, 12, 9755

First-principles study on the elastic, electronic and optical properties of all-inorganic halide perovskite solid solutions of $\text{CsPb}(\text{Br}_{1-x}\text{Cl}_x)_3$ within the virtual crystal approximation†

 Un-Hyok Ko, Jun-Hyok Ri, Jong-Hyok Jang, Chol-Hyok Ri, Un-Gi Jong 
 and Chol-Jun Yu *

All-inorganic halide perovskites have drawn significant attention for optoelectronic applications such as solar cells and light-emitting diodes due to their excellent optoelectronic properties and high stabilities. In this work, we report a systematic study on the material properties of all-inorganic bromide and chloride perovskite solid solutions, $\text{CsPb}(\text{Br}_{1-x}\text{Cl}_x)_3$, varying the Cl content x from 0 to 1 with an interval of 0.1 by applying the first-principles method within the virtual crystal approximation. The lattice constants of the cubic phase are shown to follow the linear function of mixing ratio x , verifying that Vegard's law is satisfied and the pseudopotentials of the virtual atoms are reliable. We calculate the band structures with the HSE06 hybrid functional with and without spin-orbit coupling, yielding band gaps in good agreement with experimental results, and find that the band gap increases along the quadratic function of the Cl content x . With increasing Cl content x , the elastic constants and moduli increase linearly, the effective mass of the electron and hole increase, while mobilities decrease linearly, the static dielectric constant decreases linearly, and exciton binding energy increases quadratically. We calculate the photo-absorption coefficients and reflectivity, predicting the absorption peaks shift to the ultraviolet region from bromide to chloride.

 Received 18th February 2022
 Accepted 14th March 2022

DOI: 10.1039/d2ra01084d

rsc.li/rsc-advances

1 Introduction

Recently, all-inorganic halide perovskites have attracted broad interest due to their fascinating optoelectronic properties together with improved material stability,^{1,2} and significant advances in stability have already been achieved for mixed organic-inorganic hybrid halide perovskites.³⁻⁵ In fact, this emerging class of materials has shown promising potential in widespread optoelectronic applications such as solar cells,^{6,7} light-emitting diodes,⁸⁻¹⁰ photodetectors, and lasing devices.¹¹ Among these, lead-based cesium halide perovskites with chemical formula CsPbX_3 ($X = \text{I}, \text{Br}, \text{Cl}$) have been studied most widely for advancing perovskite solar cells (PSCs) and perovskite light-emitting diodes (PLEDs). Through the numerous experimental work, PSCs based on CsPbI_3 ,¹²⁻¹⁴ CsPbBr_3 (ref. 15-17) and $\text{CsPb}(\text{I}_x\text{Br}_{1-x})_3$ (ref. 18-21) were found to exhibit relatively

high power conversion efficiencies of over $\sim 21\%$, and enhanced stability; while CsPbCl_3 has proved to be useful for PLEDs rather than PSCs due to its wider band gap.

PLEDs are expected to be promising for next generation display and lighting.⁸ It has been demonstrated that the composition dependent photoluminescence (PL) of CsPbX_3 covers the whole visible spectral range of 410-700 nm with a narrow line width of 12-42 nm and a PL quantum yield close to unity.^{22,23} In fact, CsPbI_3 was found to exhibit red luminescence with a wavelength of ~ 650 nm,²⁴ CsPbBr_3 can emit blue and green light,²⁴⁻²⁷ and CsPbCl_3 shows a purple light emission.^{28,29} Moreover, it is particularly interesting to tune the color of emitting light by making solid solutions: $\text{CsPb}(\text{Br}_{1-x}\text{Cl}_x)_3$ for a wavelength range from 420 to 480 nm,²⁸ $\text{CsPb}(\text{I}_{1-x}\text{Br}_x)_3$ for light from 520-630 nm,²³ $\text{CsPb}(\text{I}_{1-x}\text{Cl}_x)_3$ for a broader range of PL spectra.²⁹ Using CsPbBr_3 quantum dots (QDs) casted on a blue LED chip, a bright green LED was fabricated, with the PL peak and full-width at half-maximum to be tunable with a size and concentration of QDs.^{25,26} In addition, the CsPbBr_3 QDs were made in composites with mesoporous silica, and the resultant nanocomposites exhibited excellent luminescence performance.²⁷

However, developing practical PLEDs is still challenging due to the relatively short-term stability of CsPbX_3 , low external

Chair of Computational Materials Design (CMD), Faculty of Materials Science, Kim Il Sung University, PO Box 76, Pyongyang, Democratic People's Republic of Korea. E-mail: cj.yu@ryongnamsan.edu.kp

† Electronic supplementary information (ESI) available: Figures for energy-volume data fitted to EOS, frequency dependent dielectric constants calculated by BS-EXC, RPA-GW and RPA-KS methods, photo-absorption coefficients and reflectivity from RPA-GW and RPA-KS methods, and band structures from the HSE06 + SOC method. See DOI: 10.1039/d2ra01084d



quantum efficiency of the device related with its poor morphology, and relatively high cost of fabrication. For instance, the external quantum efficiencies of green and blue PLEDs based on CsPbBr₃ were reported to be very low such as 0.09% and 0.1% due to unbalanced charge injection.^{30,31} In particular, the cubic phase CsPbI₃, which is the major PL-active phase, has been found to be stable only above 315 °C and readily converts to an exclusively PL-inactive yellow phase at room temperature.^{32–34} To increase the stability, anion exchange or formation of solid solutions between the different halides was in general adopted. This also provides potential for making white PLEDs with a spectrum close to sunlight by optimizing their composition.³⁵ It was found that halide anion exchange in CsPbX₃ is remarkably fast, which is beneficial and necessary for enhancing stability, promoting facile synthesis, and in particular for ensuring color tunability in PLED applications.^{22,23,36} In exchanging and mixing halide anions, Cl and I were reported to be restricted by an unfavorable lattice mismatch,^{22,29} whereas Br–I and Br–Cl are expected to be suitable for the formation of solid solutions.

There are several first-principles studies on halide perovskite solid solutions, including all-inorganic compounds^{37–41} and organic–inorganic hybrid ones,^{42,43} using the supercell method and the efficient virtual crystal approximation (VCA) approach⁴⁴ within a density functional theory (DFT) framework. In particular, Zhou *et al.*³⁷ and Ghaithan *et al.*³⁸ reported the structural, electronic and optical properties of mixed halide perovskites CsPb(Br_{1–x}Cl_x)₃ using the supercell modeling. In this work, we investigate the elastic and optoelectronic properties of Pb-based cesium bromide and chloride perovskite solid solutions of CsPb(Br_{1–x}Cl_x)₃, gradually increasing the Cl content *x* from 0 to 1 by applying the first principles VCA approach.⁴⁴ Our work focuses on clarifying the potential of these solid solutions toward efficient and stable PLED applications.

2 Computational methods

We performed the DFT calculations using the pseudopotential plane wave method as implemented in the Quantum ESPRESSO (QE, version 6.2.0)⁴⁵ and ABINIT (version 8.8.4)^{46,47} packages. For all atomic species, we constructed the Troullier–Martins type norm-conserving pseudopotentials⁴⁸ with valence electron configurations of Cs-6s¹6p⁰, Pb-4f¹⁴5d¹⁰6s²6p², Br-3d¹⁰4s²4p⁵ and Cl-3s²3p⁵, for which the input files are provided in the pslibrary (version 1.0.0), by implementing the LD1 code included in the QE package. The exchange–correlation (XC) interaction between the valence electrons was described using the Perdew–Burke–Ernzerhof (PBE) functional⁴⁹ within the generalized gradient approximation (GGA) and the Heyd–Scuseria–Ernzerhof (HSE06) hybrid functional.⁵⁰ For virtual atoms X = Br_{1–x}Cl_x with increasing Cl content *x* from 0 to 1 with an interval of 0.1, we implemented the virtual.x code provided in the QE package.

For optimization of the CsPbX₃ unit cell in the cubic phase with a space group of *Pm3̄m*, we used the QE package with the kinetic cutoff energies of 60 Ry and 480 Ry for the plane wave basis set for the wave function and electron density and the

special *k*-points of (6 × 6 × 6). These computational parameters guarantee the accuracy of the total energy calculation as 0.5 meV per formula unit. Increasing the volume (*V*) of the unit cell evenly from 0.9*V*₀ to 1.1*V*₀, where *V*₀ is the equilibrium volume obtained by optimization, the DFT total energies (*E*) were determined by self-consistent field (SCF) calculations. We fitted the resultant *E–V* data to the natural strain equation of state (EOS) for crystalline solid⁵¹ for each value of Cl content *x*, yielding the bulk modulus and equilibrium lattice constant.

For the electronic band structures and optical properties, we applied the ABINIT package with a kinetic cutoff energy of 40 Ha and special *k*-points of (6 × 6 × 6). The HSE06 hybrid functional⁵⁰ was adopted to describe the XC interaction more precisely, where the portion of exact Hartree–Fock (HF) exchange functional was set to 0.5 for all the Cl content values. The spin–orbit coupling (SOC) effect was considered. We then calculated the effective mass and mobilities of the electron and hole for clarifying the carrier transport properties. The effective mass (*m*_e^{*}, *m*_h^{*}) could be readily obtained by post-processing the resultant band structures using the following formulae,

$$m_e^* = \left[\frac{1}{\hbar^2} \frac{\partial^2 E_{\text{CBM}}(k)}{\partial k^2} \right]^{-1}, m_h^* = \left[\frac{1}{\hbar^2} \frac{\partial^2 E_{\text{VBM}}(k)}{\partial k^2} \right]^{-1} \quad (1)$$

where *E*_{CBM}(*k*) and *E*_{VBM}(*k*) are the eigen energies as a function of wave number *k* at the conduction band minimum (CBM) and valence band maximum (VBM), respectively. The charge-carrier mobilities (*μ*_e, *μ*_h) were calculated with the deformation potential theory⁵² using the following formulae,

$$\mu_e = \frac{2\sqrt{2}\pi e\hbar^4 K}{3E'_{\text{v}}{}^2 (k_{\text{B}}T)^{3/2} (m_e^*)^{5/2}}, \mu_h = \frac{2\sqrt{2}\pi e\hbar^4 K}{3E'_{\text{c}}{}^2 (k_{\text{B}}T)^{3/2} (m_h^*)^{5/2}} \quad (2)$$

where *E*'_v = $\frac{dE_{\text{VBM}}}{d\delta}$ and *E*'_c = $\frac{dE_{\text{CBM}}}{d\delta}$ are the deformation potentials calculated using *dE*_{VBM} and *dE*_{CBM} representing the changes of VBM and CBM energies, and the lattice constant change *dδ* due to a small hydrostatic pressure, and *K* is the bulk modulus.

For the elastic properties including the elastic constants and moduli, we applied the density functional perturbation theory (DFPT)⁵³ using the PBE functional, as implemented in the ABINIT package. For the cubic phase, there are only three independent elastic constants of *C*₁₁, *C*₁₂ and *C*₄₄, from which the bulk modulus *K*, shear modulus *G*, Poisson ratio *ν* and Young's modulus *E* are given as follows,

$$K = \frac{C_{11} + 2C_{12}}{3} \quad (3)$$

$$G = \frac{5C_{44}(C_{11} - C_{12})}{8C_{44} + 6(C_{11} - C_{12})} + \frac{C_{11} - C_{12} + 3C_{44}}{10} \quad (4)$$

$$\nu = \frac{3K - 2G}{6K + 2G} \quad (5)$$

$$E = 2G(1 + \nu). \quad (6)$$

To calculate the frequency dependent dielectric function $\epsilon(\omega) = \epsilon_1(\omega) + i\epsilon_2(\omega)$, where $\epsilon_1(\omega)$ and $\epsilon_2(\omega)$ are the real and



imaginary parts of the dielectric function, we solved the Bethe–Salpeter equation including the excitonic effect (BSE-EXC) within the Tamm–Dancoff approximation, as implemented in the ABINIT package. For comparison, we also presented the results obtained within the random phase approximation (RPA) by solving the Kohn–Sham equation (RPA-KS) and GW equation (RPA-GW) with and without a local field effect (LF).⁵⁴ We note that while the KS and GW kernels do not correctly describe the strong excitonic effect within the RPA, the BS kernel is able to capture the most important physics in light absorption. From the dielectric function, the absorption coefficient $\alpha(\omega)$ and reflectivity $R(\omega)$ were calculated using the following formulae,^{39,55}

$$\alpha(\omega) = \frac{\sqrt{2}\omega}{c} \left[\sqrt{\varepsilon_1^2(\omega) + \varepsilon_2^2(\omega)} - \varepsilon_1(\omega) \right]^{\frac{1}{2}} \quad (7)$$

$$R(\omega) = \left| \frac{\sqrt{\varepsilon_1(\omega) + i\varepsilon_2(\omega)} - 1}{\sqrt{\varepsilon_1(\omega) + i\varepsilon_2(\omega)} + 1} \right|^2 \quad (8)$$

Then, the exciton binding energy E_b was obtained using the Wannier–Mott hydrogen-like model as follows,⁴²

$$E_b = \frac{m_e^* m_h^*}{m_e (m_e^* + m_h^*)} \cdot \frac{Ry}{\varepsilon_s^2} \quad (9)$$

where $Ry \approx 13.56$ eV is the Rydberg constant, m_e is the electron mass, and ε_s is the static dielectric constant that can be given by $\varepsilon_s = \varepsilon_1(\omega \rightarrow 0)$.

3 Results and discussion

We first determined the equilibrium lattice constants of Pb-based cesium bromide and chloride perovskite solid solutions of CsPbX_3 ($X = \text{Br}_{1-x}\text{Cl}_x$) with increasing Cl content x from 0 to 1. As described in the method in section 2, the E - V data was obtained by performing SCF calculations as increasing the unit cell volume evenly from $0.9V_0$ to $1.1V_0$. The obtained E - V data was fitted to the natural strain EOS at each value of Cl content x , yielding the equilibrium lattice constants and bulk moduli (see Fig. S1† for EOS curves, ESI). Fig. 1 shows the determined lattice constants and bulk moduli as functions of mixing content x .

The calculated lattice constants of 5.861 \AA for CsPbBr_3 and 5.552 \AA for CsPbCl_3 were found to be in good agreement with the experimental values of 5.874 and 5.605 \AA (ref. 35) with very small relative errors of 0.2% and 0.9%, respectively. This indicates that the pseudopotentials and computational parameters in this work are reasonable. Moreover, it was found that with increasing Cl content x , in the solid solutions the equilibrium lattice constant decreases following a linear function of $a(x) = 5.859 - 0.305x$ (\AA), which was obtained by fitting the calculated data to the first-order polynomial as shown by the dashed line in Fig. 1. Such linear varying tendency of lattice constants indicates that Vegard's law can be reproduced well with the VCA approach⁴⁴ for all-inorganic halide perovskite solid solutions. It is worth noting that the lattice constant difference between CsPbBr_3 and CsPbCl_3 is relatively small with only a relative

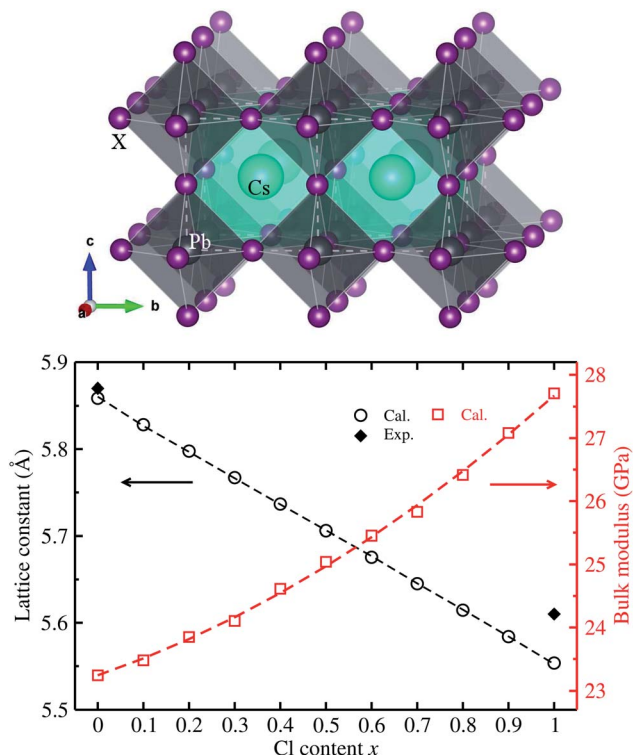


Fig. 1 Ball-and-polyhedral view of the crystalline structure of cubic CsPbX_3 ($X = \text{Br}_{1-x}\text{Cl}_x$) (top panel), where the white-colored dashed lines indicate the unit cell; and calculated lattice constants and bulk moduli are functions of Cl content x (bottom panel), where the dashed lines represent the fitted first- and second-order polynomials. Experimental values for lattice constants are from ref. 35.

difference of 5%, implying the fast halide anion exchange between Br and Cl anions.²² On the other hand, the bulk modulus was found to increase following a quadratic function of $K(x) = 23.242 + 2.464x + 1.947x^2$ (GPa) with increasing Cl content x . Such quadratic functions for bulk moduli were also found in other halide perovskite solid solutions within VCA.^{39,42,43} The decrease of lattice constants and increase of bulk moduli are mainly attributed to strengthening of the Pb–X bond, indicating the stability increase in CsPbX_3 ($X = \text{Br}_{1-x}\text{Cl}_x$) with increasing Cl content x .

Using the optimized unit cells, we then calculated the electronic band structures of $\text{CsPb}(\text{Br}_{1-x}\text{Cl}_x)_3$ with increasing Cl content x . With a choice of exchange–correlation functional, we remind that the PBE-GGA functional underestimates the band gap while the HSE06 hybrid functional gives band gaps in good agreement with experimental for all-inorganic halide perovskites, and include the SOC effect which severely reduces the band gaps.^{56,57} It is worth noting that SOC can be improved using better core pseudopotentials or explicitly introducing SOC in the Hamiltonian.⁵⁸ In this work, we used the HSE06 hybrid functional with the fixed portion (0.5) of exact HF exchange interaction with and without the SOC effect, to calculate the band structures and band gaps.

Fig. 2 shows the band structures and band gaps as a function of mixing ratio calculated with the HSE06 functional without the SOC effect. In Fig. 2(a), one can see a similar dispersion



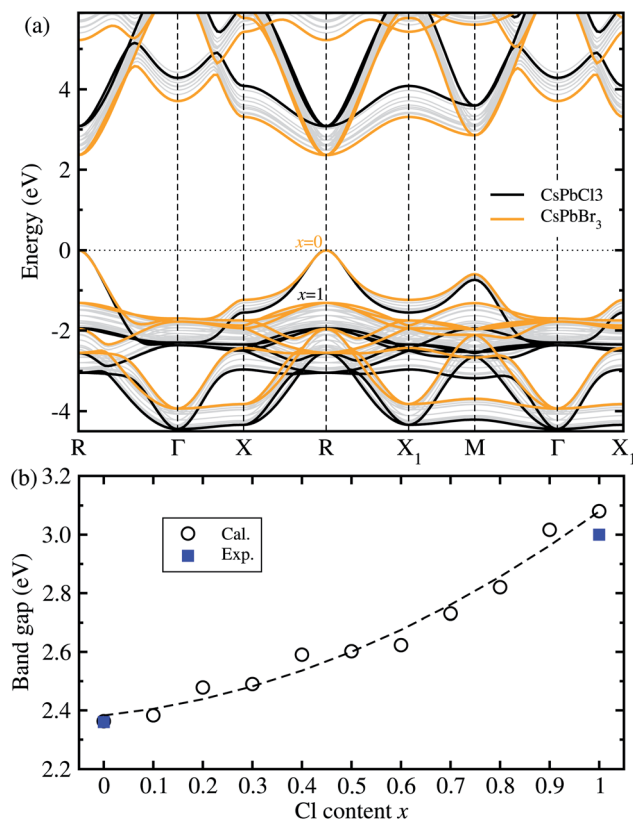


Fig. 2 (a) Band structures of cubic CsPbX_3 ($X = \text{Br}_{1-x}\text{Cl}_x$) with increasing Cl mixing ratio x from 0 to 1, calculated using the HSE06 hybrid functional with the fixed portion of exact HF exchange interaction as 0.5, where the valence band maximum is set to zero. (b) Band gaps as a function of mixing ratio, where the dashed line represents the fitting line to the quadratic polynomial. Experimental values are from ref. 15 and ref. 35 for $x = 0$ and 1, respectively.

feature overall, and at the direct band gaps at the R point, for all the perovskite solid solutions with the varying mixing ratio values without any anomaly. It was found that with increasing Cl content x from 0 to 1 in $\text{CsPb}(\text{Br}_{1-x}\text{Cl}_x)_3$ the VBM moves gradually downwards while the CBM moves upwards at the R point, resulting in the gradual increase of band gap. We note that such a direct transition is more beneficial to absorption and radiation of light than the indirect transition. On the other hand, the HSE06 + SOC method yielded the underestimated band gaps due to a splitting and down-shift of the conduction band known as the Rashba effect (see Fig. S4, ESI†).

For the two extreme compounds at $x = 0$ (CsPbBr_3) and $x = 1$ (CsPbCl_3), the direct band gaps were calculated to be 2.36 eV and 3.08 eV, which are in good agreement with the experimental values of 2.36 eV (ref. 15) and 3.03 eV (ref. 35), respectively (see Fig. S5† for comparison between HSE06 and HSE06 + SOC, ESI†). The absolute deviation values with HSE06 are 0 eV and 0.05 eV, indicating that the HSE06 functional is most reliable in reproducing and predicting band gaps of all-inorganic halide perovskites. Fig. 2(b) shows the variation tendency of band gaps as a function of Cl content x in the solid solutions. Like other halide perovskite solid solutions, we fitted the calculation data

to the quadratic function, resulting in $E_g(x) = 2.383 + 0.174x + 0.522x^2$ (eV). In this function, the bowing parameter reflecting the qualitative miscibility between the components of solid solution was found to be 0.52 eV, which is slightly higher than the experimental value of 0.47 eV for $\text{CsPb}(\text{I}_{1-x}\text{Br}_x)_3$.³⁹ When compared with the organic-inorganic hybrid solid solutions, this value is smaller than 0.87 eV for $\text{MAPb}(\text{I}_{1-x}\text{Cl}_x)_3$ (ref. 43) but larger than 0.18 eV for $\text{MAPb}(\text{I}_{1-x}\text{Br}_x)_3$.⁴² From the analysis of the bowing parameter, we induce that the compositional disorder and miscibility between CsPbBr_3 and CsPbI_3 are reasonable, being better than the organic-inorganic hybrid counterpart. Considering that the composition-dependent band gap indicates the tunability of color emission in a PLED device, one can predict the luminescence peak wavelength of the Br-Cl perovskite solid solution at a certain mixing ratio using this function.

Next, we considered the elastic properties including the elastic constants and moduli, since the elastic properties reflect the information on the binding strength, anisotropy and structural stability of the crystal. Fig. 3 shows the elastic constants and moduli obtained by applying the DFPT method using the PBE functional. The three independent components of elastic constant show increasing tendencies with the increase in Cl content x along the linear functions of $C_{11} = 55.275 + 11.283x$ (GPa), $C_{12} = 6.217 + 1.979x$ (GPa) and $C_{44} = 3.222 + 0.598x$ (GPa). With increasing Cl content in the solid solution, the bond length between the Pb cation and halide anion becomes shorter as the lattice constant decreases, resulting in enhancement of binding strength and thus structural stability. As such, the bulk modulus K , shear modulus G and Young's modulus E , which are estimated from the elastic constants, were also found to linearly increase following $K = 22.570 + 5.081x$ (GPa), $G = 2.424 + 0.450x$ (GPa), and $E = 7.022 + 1.312x$ (GPa), respectively. We confirmed that the calculated bulk moduli for the two end compounds are in good agreement with the previous theoretical work.⁵⁵ We also estimated the anisotropy factor as $A = 2C_{44}/(C_{11} - C_{12})$, which was found to be between 0.12 and 0.14 for $\text{CsPb}(\text{Br}_{1-x}\text{Cl}_x)_3$ with $x = 0-1$, with severe deviation from 1 for an isotropic crystal.

For optoelectronic applications like solar cells and LEDs, the effective mass and mobilities of the electron and hole are of great importance, and are prerequisite factors for perovskites to become the active layers in any device.^{55,59,60} The effective mass of charge carriers was obtained from the detailed band structures (see Fig. 2) calculated with the HSE06 functional by applying the parabolic approximation around the R point of the conduction and valence bands using eqn (1). To evaluate the carrier mobilities using eqn (2), we recalculated the band structures by varying the lattice constant from 99.8% to 100.2% with an interval of 0.1% and then obtained the deformation potentials as the gradients of the CBM and VBM energies with respect to the lattice constant change at each value of Cl content x .

Fig. 4 shows the calculated effective mass and mobilities of the electron and hole as functions of Cl content x in solid solutions of CsPbX_3 . For the two extreme compounds, the effective mass of electron and hole were calculated to be $m_e^* = 0.078m_e$ and $m_h^* = 0.142m_e$ for CsPbBr_3 and



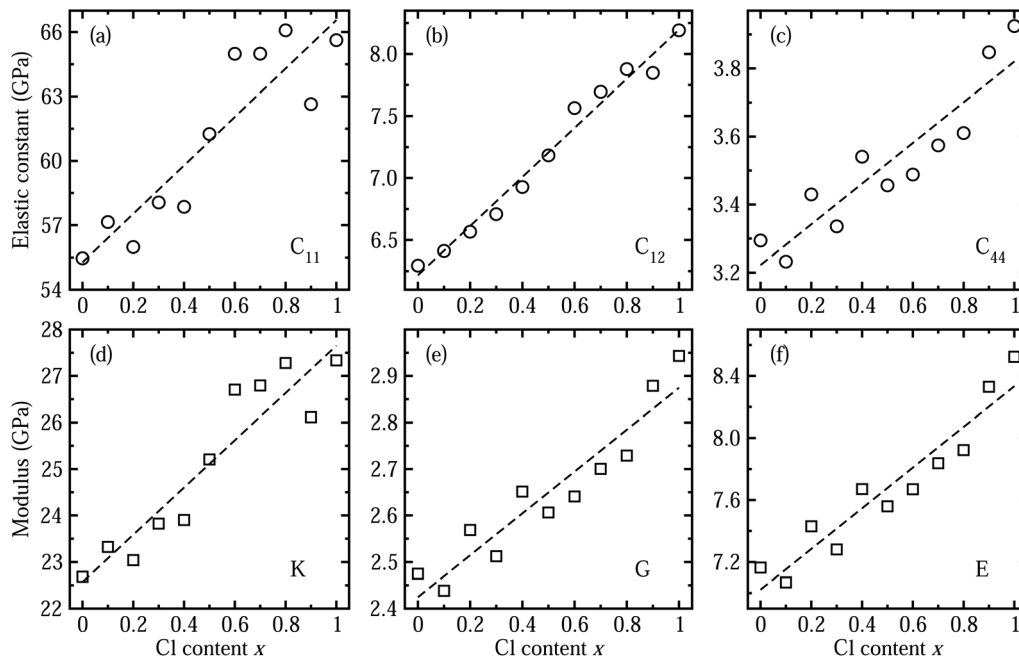


Fig. 3 Calculated elastic constants of (a) C_{11} , (b) C_{12} , and (c) C_{44} of halide perovskite solid solutions of CsPbX_3 ($X = \text{I}_{1-x}\text{Br}_x$) as functions of Cl content x , by applying the DFPT method. (d) Bulk modulus K , (e) shear modulus G , and (f) Young's modulus, obtained from the elastic constants. Dashed lines indicate the linear function fit.

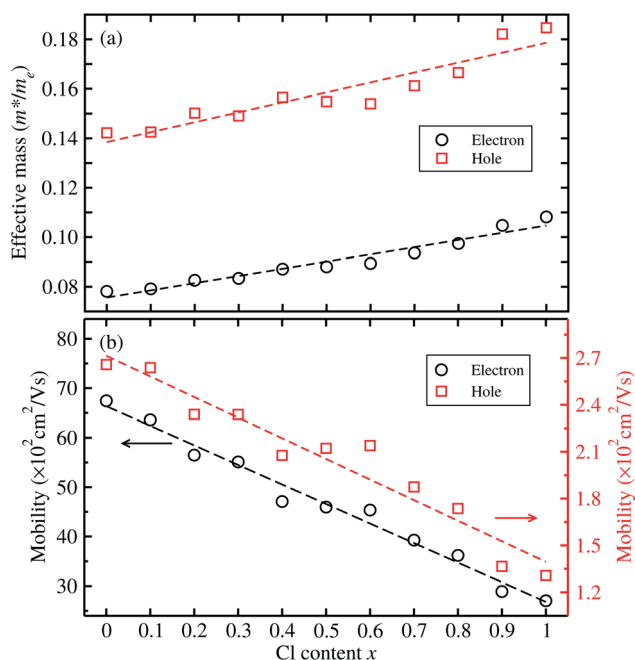


Fig. 4 (a) Effective mass of electron and hole calculated from the band structures with the HSE06 functional, and (b) electron and hole mobilities calculated from the effective mass, bulk moduli and deformation potentials, as a function of Cl content x in solid solutions of $\text{CsPb}(\text{Br}_{1-x}\text{Cl}_x)_3$. Dashed lines indicate lines of fit.

$m_e^* = 0.108m_e$ and $m_h^* = 0.185m_e$ for CsPbCl_3 , which are clearly smaller than $m_e^* = 0.15m_e$ and $m_h^* = 0.20m_e$ for CsPbI_3 .⁵⁵ When compared with the organic-inorganic hybrid

counterparts of MAPbBr_3 and MAPbCl_3 , where MA is the methylammonium (CH_3NH_3) cation, CsPbBr_3 has a much lighter effective mass than $m_e^* = 0.21m_e$ and $m_h^* = 0.23m_e$ for MAPbBr_3 (ref. 42) and CsPbCl_3 also has a lower effective mass than $m_e^* = 0.34m_e$ and $m_h^* = 0.47m_e$ for MAPbCl_3 .⁴³ These indicate that both CsPbBr_3 and CsPbCl_3 have better charge carrier transport properties than CsPbI_3 , MAPbBr_3 and MAPbCl_3 . Since the effective mass in CsPbCl_3 is larger than in CsPbBr_3 , it can be expected that mixing bromide with chloride in a perovskite, forming solid solutions, will induce an increase in effective mass but will still be lower than CsPbCl_3 . In fact, it was revealed that both the electron and hole effective mass of solid solutions increases with increasing Cl content x along the linear functions of $m_e^* = (0.076 + 0.029x)m_e$ and $m_h^* = (0.138 + 0.040x)m_e$, respectively. We note that the electrons are almost twice as light as the holes in the active layer of the device after their generation by photon excitation or charge injection in the $\text{CsPb}(\text{Br}_{1-x}\text{Cl}_x)_3$ -based PSCs or PLEDs. In accordance with the change tendencies of effective mass, the charge carrier mobilities were found to decrease with increasing Cl content along the linear functions of $\mu_e = (66.360 - 39.548x) \times 10^2 \text{ cm}^2 \text{ V}^{-1} \text{ s}^{-1}$ and $\mu_h = (2.714 - 1.320x) \times 10^2 \text{ cm}^2 \text{ V}^{-1} \text{ s}^{-1}$. Again, it was found that the electron mobilities are much larger than the hole mobilities.

For optical properties, we calculated the frequency dependent dielectric function of solid solutions of CsPbX_3 ($X = \text{Br}_{1-x}\text{Cl}_x$). To this end, we solved the Bethe-Salpeter equation (BSE) incorporating the excitonic effect (EXC), *i.e.*, interactions between electron and hole. Due to the cubic symmetry of CsPbX_3 , we averaged the identical xx , yy , and zz components of



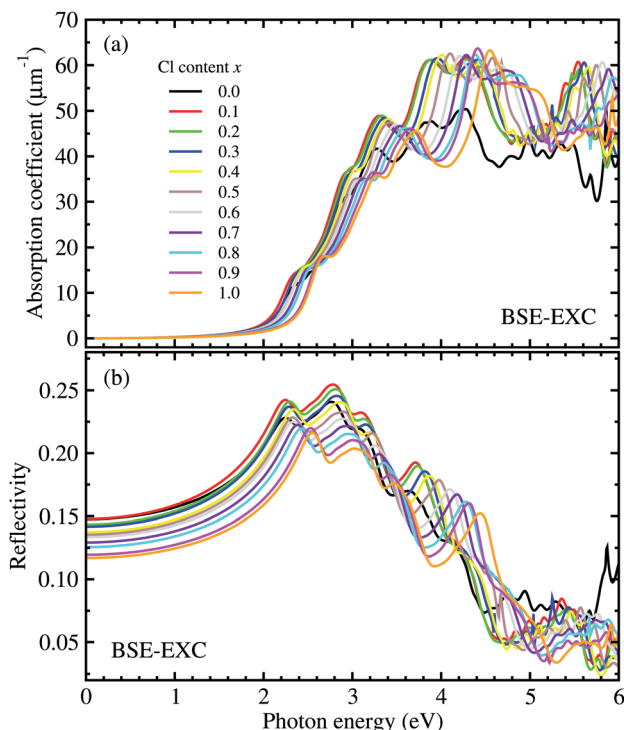


Fig. 5 (a) The photo-absorption coefficient and (b) reflectivity of perovskite solid solutions of $\text{CsPb}(\text{Br}_{1-x}\text{Cl}_x)_3$ with Cl content $x = 0-1$ as functions of photon energy, are obtained from the frequency dependent dielectric functions calculated by solving the Bethe-Salpeter equation (BSE) including the excitonic effect (EXC).

the dielectric tensor (see Fig. S2† for real and imaginary parts of the dielectric functions, ESI). For comparison, the frequency dependent dielectric constants were also calculated using different levels of theory such as RPA-KS and RPA-GW (see Fig. S3, ESI†). The photo-absorption coefficients and reflectivity were obtained from these dielectric functions using eqn (7) and (8). Fig. 5 shows the calculated photo-absorption coefficients and reflectivity of solid solutions of $\text{CsPb}(\text{Br}_{1-x}\text{Cl}_x)_3$ with increasing Cl content x from 0 to 1 with an interval of 0.1. The absorption onset was observed to be shifted to the ultraviolet region when increasing the Cl content, which coincides with the tendency of band gap change as discussed above.

From the real part of the dielectric function calculated by the BS-EXC approach or RPA-KS-NLF and RPA-KS-LF approaches, we extracted the static dielectric constant as $\epsilon_s = \epsilon_1(\omega \rightarrow 0)$. For CsPbBr_3 and CsPbCl_3 , the static dielectric constants were determined to be 5.05 and 4.16 from the BS-EXC results, which are slightly smaller than the previous theoretical values of 4.20 and 3.66 obtained with PBE + SOC.⁵⁵ These values are also slightly smaller than those of the organic-inorganic hybrid counterparts of MAPbBr_3 (3.80)⁴² and MAPbCl_3 (3.11).⁴³ When increasing the Cl content x , we found the increasing tendency of the static dielectric constants along the linear function of $\epsilon = 5.124 - 0.928x$, as shown in Fig. 6(a). In this figure, we also show the DFPT calculation results for comparison. It was found that the RPA-KS-NLF approach gave slightly larger or similar values with a linear

function of $\epsilon = 5.487 - 1.375x$, whereas the RPA-KS approach including the local field effect, yielded much smaller values with a linear function of $\epsilon = 4.740 - 1.194x$.

Finally, we determined the exciton binding energy E_b from the calculated effective mass and static dielectric constants with BS-EXC using eqn (9). The exciton binding energy implies the stability of the exciton comprised of photo-generated electron and hole; a lower value means faster carrier dissociation, being favourable for the solar cell or LED application. For CsPbBr_3 , E_b was found to be 26.9 meV in good agreement with the experimental value of 26 meV.⁶¹ The calculated value of 53.7 meV for CsPbCl_3 is comparable with previous experimental and theoretical values.^{36,55,61} These values can be thought of as relatively small, indicating the weak binding in the exciton, *i.e.*, Mott-Wannier exciton, which is beneficial for the fast dissociation of the exciton into free charge carriers. As shown in Fig. 6(b), the calculated values of solid solutions of $\text{CsPb}(\text{Br}_{1-x}\text{Cl}_x)_3$ show an increasing tendency with increasing Cl content x , according to the quadratic function of $E_b = 27.389 + 2.473x + 23.711x^2$ (meV). Such increasing tendency is reasonable because the effective mass of the electron and hole become smaller and the static dielectric constants decrease with increasing Cl content. In Table 1, we summarize the fitted functions for the calculated data in comparison with other

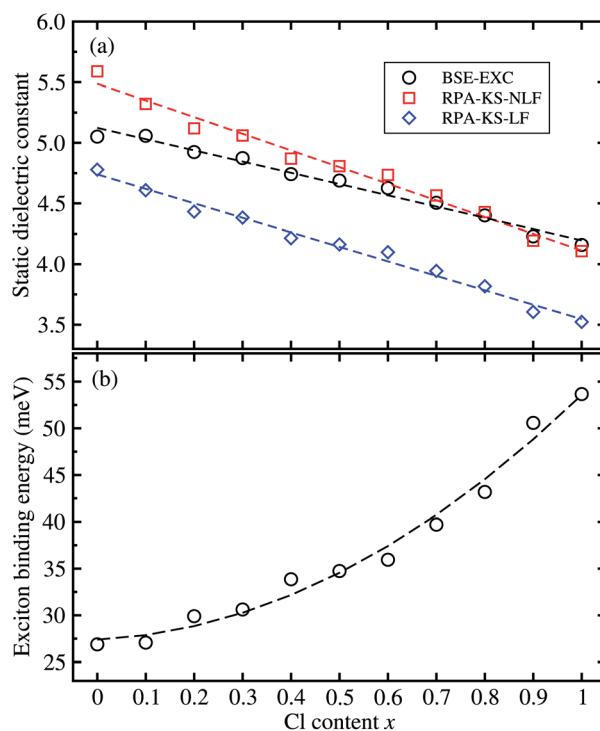


Fig. 6 (a) Static dielectric constants as a function of the Cl content x in solid solutions of $\text{CsPb}(\text{Br}_{1-x}\text{Cl}_x)_3$, calculated by solving the Bethe-Salpeter equation including the excitonic effect (BS-EXC) or by density functional perturbation theory within the random phase approximation in the Kohn-Sham approach (RPA-KS) without the local field effect (NLF) and with LF. (b) The exciton binding energy is obtained from the BS-EXC result.



Table 1 Fitted functions obtained by regressing data calculated within VCA to the first- or second-order polynomials in comparison with the previous data for other halide perovskite solid solutions of CsPb(Br_{1-x}Br_x)₃,³⁹ MAPb(I_{1-x}Br_x)₃,⁴² and MAPb(I_{1-x}Cl_x)₃ (ref. 43)

	CsPb(Br _{1-x} Cl _x) ₃	CsPb(I _{1-x} Br _x) ₃ (ref. 39)	MAPb(I _{1-x} Br _x) ₃ (ref. 42)	MAPb(I _{1-x} Cl _x) ₃ (ref. 43)
Lattice constant (Å)	5.859 - 0.305x	6.242 - 0.378x	6.420 - 0.333x	6.310 - 0.716x
Bulk modulus (GPa)	23.242 + 2.464x + 1.947x ²			10.627 + 5.492x
Band gap, HSE06 (eV)	2.383 + 0.174x + 0.522x ²	2.245 + 0.067x + 0.071x ²		
PBE or PBEsol		1.759 + 0.012x + 0.032x ²	1.542 + 0.374x + 0.185x ²	1.521 + 0.269x + 0.873x ²
Electron effective mass (m _e)	0.076 + 0.029x			0.199 + 0.140x
Hole effective mass (m _e)	0.138 + 0.040x			0.231 + 0.203x
Static dielectric constant	5.124 - 0.928x	5.077 - 0.451x	5.230 - 1.430x	5.698 - 2.593x
Exciton binding energy (meV)	27.389 + 2.473x + 23.711x ²		45 + 57x	55 - 36x + 25.3x ²
Elastic constant C ₁₁ (GPa)	55.275 + 11.283x			
Elastic constant C ₁₂ (GPa)	6.217 + 1.979x			
Elastic constant C ₄₄ (GPa)	3.222 + 0.598x			
Electron mobility (× 10 ² cm ² V ⁻¹ s ⁻¹)	66.360 - 39.548x			
Hole mobility (× 10 ² cm ² V ⁻¹ s ⁻¹)	2.714 - 1.320x			

halide perovskite solid solutions, which will be helpful for material designers and engineers.

4 Conclusions

In this work we have performed first-principles calculations within the virtual crystal approximation to systematically investigate the structural, elastic, electronic and optical properties of all-inorganic halide perovskite solid solutions of CsPb(Br_{1-x}Cl_x)₃ in the cubic phase with varying Cl content *x*. Confirming that the calculated lattice constants of the two extreme compounds were in good agreement with the experimental values, we found that the equilibrium lattice constants of the solid solutions increased along the linear function of $a(x) = 5.859 - 0.305x$ (Å) with increasing Cl content *x*, indicating the satisfaction of Vegard's law and reliability of the pseudopotentials of the virtual atoms. Our calculations revealed that the band gaps calculated with HSE06 increased quadratically according to the function of $E_g(x) = 2.38 + 0.17x + 0.52x^2$, predicting the luminescence peak wavelength of the solid solution at a certain mixing ratio. We found that the elastic constants and moduli exhibited a monotonic increasing tendency with the increase of Cl content, implying that the binding strength and structural stability can be enhanced upon mixing bromide with chloride. For the charge-carrier transport properties, we calculated the effective mass of electron and hole, showing the linear increasing tendencies of $m_e^*(x) = (0.076 + 0.029x)m_e$ and $m_h^*(x) = (0.138 + 0.040x)m_e$ and thereby the linear decreasing tendencies for mobilities. We then computed the frequency dependent dielectric functions with BS-EXC and the photo-absorption coefficients, finding that the absorption peaks were shifted to the ultraviolet region with increasing Cl content. Finally, we found that the static dielectric constants decreased along the linear function of $\epsilon(x) = 5.124 - 0.928x$, while the exciton binding energies increased according to the quadratic function of $E_b = 27.39 + 2.47x + 23.71x^2$ (meV), revealing the weak binding strength of exciton and its fast dissociation into free carriers. We believe that this work can provide useful guidance for developing active materials based on halide perovskites for PLEDs.

Author contributions

Un-Hyok Ko and Chol-Jun Yu developed the original project, performed the calculations and drafted the first manuscript. Jun-Hyok Ri, Jong-Hyok Jang, Chol-Hyok Ri and Un-Gi Jong assisted with the DFT calculations and the post-processing of calculation results, and contributed to useful discussions. Chol-Jun Yu supervised the work. All authors reviewed the manuscript.

Conflicts of interest

There are no conflicts to declare.

Acknowledgements

This work is supported as part of the fundamental research project "Design of New Energy Materials" (No. 2021-5) funded by the State Commission of Science and Technology, DPR Korea. Computation in this work was done on the HP Blade System C7000 (HP BL460c) that is owned and managed by the Faculty of Materials Science, Kim Il Sung University.

References

- X. Li, F. Cao, D. Yu, J. Chen, Z. Sun, Y. Shen, Y. Zhu, L. Wang, Y. Wei, Y. Wu and H. Zeng, *Small*, 2017, **13**, 1603996.
- C.-J. Yu, *JPhys Energy*, 2019, **1**, 022001.
- N. Li, Z. Zhu, C.-C. Chueh, H. Liu, B. Peng, A. Petrone, X. Li, L. Wang and A. K.-Y. Jen, *Adv. Energy Mater.*, 2017, **7**, 1601307.
- H. Zhang, H. Wang, S. T. Williams, D. Xiong, W. Zhang, C.-C. Chueh and A. K.-Y. Jen, *Adv. Mater.*, 2017, **29**, 1606608.
- A. Rajagopal, R. J. Stoddard, S. B. Jo, H. W. Hillhouse and A. K.-Y. Jen, *Nano Lett.*, 2018, **18**, 3985-3993.
- T. Leijtens, K. Bush, R. Cheacharoen, R. Beal, A. Bowring and M. D. McGehee, *J. Mater. Chem. A*, 2017, **5**, 11483-11500.
- W. Xiang and W. Tress, *Adv. Mater.*, 2019, 1902851.
- C. Ge, Q. Fang, H. Lin and H. Hu, *Front. Mater.*, 2021, **8**, 635025.
- J. Luo, X. Wang, S. Li, J. Liu, Y. Guo, G. Niu, L. Yao, Y. Fu, L. Gao, Q. Dong, *et al.*, *Nat. Lett.*, 2018, **563**, 541-545.



- 10 K. Lin, J. Xing, L. N. Quan, F. P. G. de Arquer, X. Gong, J. Lu, L. Xie, W. Zhao, D. Zhang, C. Yan, *et al.*, *Nat. Lett.*, 2018, **562**, 245–248.
- 11 X. Wang, H. Zhou, S. Yuan, W. Zheng, Y. Jiang, X. Zhuang, H. Liu, Q. Zhang, X. Zhu, X. Wang and A. Pan, *Nano Res.*, 2017, **10**, 3385–3395.
- 12 A. Swarnkar, A. R. Marshall, E. M. Sanehira, B. D. Chernomordik, D. T. Moore, J. A. Christians, T. Chakrabarti and J. M. Luther, *Science*, 2016, **354**, 92–95.
- 13 T. Zhang, M. I. Dar, G. Li, F. Xu, N. Guo, M. Grätzel and Y. Zhao, *Sci. Adv.*, 2017, **3**, e1700841.
- 14 E. M. Sanehira, A. R. Marshall, J. A. Christians, S. P. Harvey, P. N. Ciesielski, L. M. Wheeler, P. Schulz, L. Y. Lin, M. C. Beard and J. M. Luther, *Sci. Adv.*, 2017, **3**, eaao4204.
- 15 M. Kulbak, D. Cahen and G. Hodes, *J. Phys. Chem. Lett.*, 2015, **6**, 2452–2456.
- 16 C.-X. Qian, Z.-Y. Deng, K. Yang, J. Feng, M.-Z. Wang, Z. Yang, S. Liu and H.-J. Feng, *Appl. Phys. Lett.*, 2018, **112**, 093901.
- 17 X. Liu, X. Tan, Z. Liu, H. Ye, B. Sun, T. Shi, Z. Tang and G. Liao, *Nano Energy*, 2019, **56**, 184.
- 18 Z. Guo, S. Teo, Z. Xu, C. Zhang, Y. Kamata, S. Hayase and T. Ma, *J. Mater. Chem. A*, 2019, **7**, 1227–1232.
- 19 W. Chen, H. Chen, G. Xu, R. Xue, S. Wang and Y. Li, *Joule*, 2019, **3**, 191–204.
- 20 F. Zhao, J. Liu, X. Gao, X. Qin, X. Qiu, X. Liu, T. He and R. Chen, *J. Phys. Chem. C*, 2019, **123**, 9538–9543.
- 21 Z. Li, X. Liu, J. Xu, Y. Liao, H. Zhao, B. Zhang, S. F. Liu and J. Yao, *J. Phys. Chem. Lett.*, 2019, **10**, 4587–4595.
- 22 G. Nedelcu, L. Protesescu, S. Yakunin, M. I. Bodnarchuk, M. J. Grotevent and M. V. Kovalenko, *Nano Lett.*, 2015, **15**, 5635–5640.
- 23 L. Protesescu, S. Yakunin, M. I. Bodnarchuk, F. Krieg, R. Caputo, C. H. Hendon, R. X. Yang, A. Walsh and M. V. Kovalenko, *Nano Lett.*, 2015, **15**, 3692–3696.
- 24 Y.-X. Zhang, H.-Y. Wang, Z.-Y. Zhang, Y. Zhang, C. Sun, Y.-Y. Yue, L. Wang, Q.-D. Chen and H.-B. Sun, *Phys. Chem. Chem. Phys.*, 2017, **19**, 1920–1926.
- 25 W. Chen, X. Xin, Z. Zang, X. Tang, C. Li, W. Hu, M. Zhou and J. Du, *Phys. Chem. Chem. Phys.*, 2017, **19**, 115–120.
- 26 H. Chen, A. Guo, J. Zhu, L. Cheng and Q. Wang, *Appl. Surf. Sci.*, 2019, **465**, 656–664.
- 27 X. Di, L. Shen, J. Jiang, M. He, Y. Cheng, L. Zhou, X. Liang and W. Xiang, *J. Alloys Compd.*, 2017, **729**, 526–532.
- 28 J. Song, J. Li, X. Li, L. Xu, Y. Dong and H. Zeng, *Adv. Mater.*, 2015, **27**, 7162–7167.
- 29 N. J. L. K. Davis, F. J. de Peña, M. Tabachnyk, J. M. Richter, R. D. Lamboll, E. P. Booker, F. W. R. Rivarola, J. T. Griffiths, C. Ducati, S. M. Menke, *et al.*, *J. Phys. Chem. C*, 2017, **121**, 3790–3796.
- 30 D. Yang, Y. Zou, P. Li, Q. Liu, L. Wu, H. Hu, Y. Xu, B. Sun, Q. Zhang and S.-T. Lee, *Nano Energy*, 2018, **47**, 235–242.
- 31 S. Zhuang, X. Ma, D. Hu, X. Dong, Y. Zhang and B. Zhang, *Optical Mater.*, 2018, **77**, 25–29.
- 32 C. C. Stoumpos, C. D. Malliakas and M. G. Kanatzidis, *Inorg. Chem.*, 2013, **52**, 9019–9038.
- 33 A. Marronnier, H. Lee, B. Geffroy, J. Even, Y. Bonnassieux and G. Roma, *J. Phys. Chem. Lett.*, 2017, **8**, 2659–2665.
- 34 A. Marronnier, G. Roma, S. Boyer-Richard, L. Pedesseau, J.-M. Jancu, Y. Bonnassieux, C. Katan, C. C. Stoumpos, M. G. Kanatzidis and J. Even, *ACS Nano*, 2018, **12**, 3477–3486.
- 35 Q. A. Akkerman, V. D’Innocenzo, S. Accornero, A. Scarpellini, A. Petrozza, M. Prato and L. Manna, *J. Am. Chem. Soc.*, 2015, **137**, 10276–10281.
- 36 S.-T. Ha, R. Su, J. Xing, Q. Zhang and Q. Xiong, *Chem. Sci.*, 2017, **8**, 2522–2536.
- 37 Z. Zhou, Y. Cui, H.-X. Deng, L. Huang, Z. Wei and J. Li, *Appl. Phys. Lett.*, 2017, **110**, 113901.
- 38 H. M. Ghaithan, Z. A. Alahmed, S. M. H. Qaid and A. S. Aldwayyan, *Materials*, 2020, **13**, 4944.
- 39 C.-J. Yu, U.-H. Ko, S.-G. Hwang, Y.-S. Kim, U.-G. Jong, Y.-H. Kye and C.-H. Ri, *Phys. Rev. Mater.*, 2020, **4**, 045402.
- 40 R. A. Evarestov, E. A. Kotomin, A. Senocrate, R. K. Kremer and J. Maier, *Phys. Chem. Chem. Phys.*, 2020, **22**, 3914–3920.
- 41 U.-G. Jong, C.-J. Yu, Y.-H. Kye, Y.-S. Kim, C.-H. Kim and S.-G. Ri, *J. Mater. Chem. A*, 2018, **6**, 17994–18002.
- 42 U.-G. Jong, C.-J. Yu, J.-S. Ri, N.-H. Kim and G.-C. Ri, *Phys. Rev. B*, 2016, **94**, 125139.
- 43 U.-G. Jong, C.-J. Yu, Y.-M. Jang, G.-C. Ri, S.-N. Hong and Y.-H. Pae, *J. Power Sources*, 2017, **350**, 65–72.
- 44 C.-J. Yu and H. Emmerich, *J. Phys.: Condens. Matter*, 2007, **19**, 306203.
- 45 P. Giannozzi, S. Baroni, N. Bonini, M. Calandra, R. Car, C. Cavazzoni, D. Ceresoli, G. L. Chiarotti, M. Cococcioni, I. Dabo, *et al.*, *J. Phys.: Condens. Matter*, 2009, **21**, 395502.
- 46 X. Gonze, F. Jollet, F. A. Araujo, D. Adams, B. Amadon, T. Applencourt, C. Audouze, J.-M. Beuken, J. Bieder, A. Bokhanchuk, *et al.*, *Comput. Phys. Commun.*, 2016, **205**, 106.
- 47 X. Gonze, B. Amadon, P. M. Anglade, J.-M. Beuken, F. Bottin, P. Boulanger, F. Bruneval, D. Caliste, R. Caracas, M. Cote, *et al.*, *Comput. Phys. Commun.*, 2009, **180**, 2582–2615.
- 48 N. Troullier and J. L. Martins, *Phys. Rev. B: Condens. Matter Mater. Phys.*, 1991, **43**, 1993–2006.
- 49 J. P. Perdew, K. Burke and M. Ernzerhof, *Phys. Rev. Lett.*, 1996, **77**, 3865.
- 50 J. Heyd and G. E. Scuseria, *J. Chem. Phys.*, 2004, **121**, 1187.
- 51 J.-P. Poirier and A. Tarantola, *Phys. Earth Planet. Inter.*, 1998, **109**, 1–8.
- 52 J. Bardeen and W. Shockley, *Phys. Rev.*, 1950, **80**, 72.
- 53 X. Wu, D. Vanderbilt and D. R. Hamann, *Phys. Rev. B: Condens. Matter Mater. Phys.*, 2005, **72**, 035105.
- 54 M. Kumar, A. Singh, D. Gill and S. Bhattacharya, *J. Phys. Chem. Lett.*, 2021, **12**, 5301–5307.
- 55 Y. Ying, X. Luo and H. Huang, *J. Phys. Chem. C*, 2018, **122**, 17718–17725.
- 56 U.-G. Jong, C.-J. Yu, Y.-H. Kye, Y.-G. Choe, W. Hao and S. Li, *Inorg. Chem.*, 2019, **58**, 4134–4140.
- 57 U.-G. Jong, C.-J. Yu, Y.-S. Kim, Y.-H. Kye and C.-H. Kim, *Phys. Rev. B*, 2018, **98**, 125116.
- 58 A. Petrone, D. B. Williams-Young, S. Sun, T. F. Stetina and X. Li, *Eur. Phys. J. B*, 2018, **91**, 169.
- 59 J. Feng and B. Xiao, *J. Phys. Chem. C*, 2014, **118**, 19655–19660.
- 60 T. Zhao, W. Shi, J. Xi, D. Wang and Z. Shuai, *Sci. Rep.*, 2016, **7**, 19968.
- 61 N. Mondal and A. Samanta, *Nanoscale*, 2017, **9**, 1878–1885.

